analytical chemistry

Article

Cite This: *Anal. Chem.* 2019, 91, 1619−1626

pubs.acs.org/ac

Dynamic Microfluidic Cytometry for Single-Cell Cellomics: High-Throughput Probing Single-Cell-Resolution Signaling

Peng Chen,[†] Shuangqian Yan,[†] Jie Wang, Yiran Guo, Yue Dong, Xiaojun Feng, Xuemei Zeng, Yiwei Li, Wei Du, and Bi-Feng Liu*

The Key Laboratory for Biomedical Photonics of MOE at Wuhan National Laboratory for Optoelectronics−Hubei Bioinformatics & Molecular Imaging Key Laboratory, Systems Biology Theme, Department of Biomedical Engineering, College of Life Science and Technology, Huazhong University of Science and Technology, Wuhan 430074, China

Supporting Information

ABSTRACT: Cell signaling is a fast, dynamic, and complex process, which controls a variety of critical physiological functions. Methods to investigate such dynamic information, however, suffer from limited throughput in the single-cell level and a lack of precise fluid manipulation. Herein, we present a new strategy, termed dynamic microfluidic cytometry (DMC), for high-throughput probing of G protein-coupled receptor (GPCR) signaling in single-cell resolution (single-cell cellomics analysis) by creatively applied cyclical cell trapping, stimulating, and releasing automatically. Dose−response curves and half-maximal effective concentration (EC50) values for HeLa cells treated with adenosine triphosphate (ATP), histamine (HA), and acetylcholine chloride (ACH) were successfully obtained in the single-cell level. High-throughput single-cell dynamic signaling was further implemented by sequential or simultaneous stimulation, which revealed that different mechanisms were working in triggering intracellular calcium release. In addition, simultaneous stimulation to two different types of cells, HeLa and NIH-3T3 cells, was also successfully realized, which was crucial for online comparison of dynamic signaling of different types of cells. We believe that the proposed DMC provides a versatile means for high-throughput probing single-cell dynamic signaling, which is potentially useful in chemical biology, cell biology, and pharmacology.

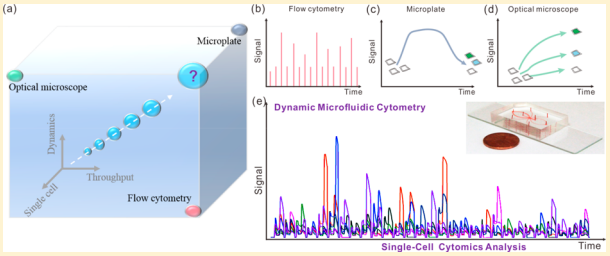

The completion of Human Genome Project and rapid development on genomics, transcriptomics, proteomics, and metabolomics in the past 2 decades have made great impacts on current life science.[1] However, most of the advancements were achieved at the cell population or tissues level with an ignorance of cell heterogeneity. The question of how the molecular blocks (genes, mRNA, proteins, and metabolites) build the unique individual cells attracts increasing attention these days. Thus, new technologies for single-cell-resolution analysis, for example, single-cell sequencing,[2−6] single-cell proteomics, or metabolomics,[7−13] are highly desired and growing rapidly.[14] Especially, with the progress of the Human Cell Atlas program,[15−17] the burgeoning cytomics represents a brand-new challenge aiming to determine multiple biochemical heterogeneity features in cellular systems at the single-cell resolution, which will be of great significance to discover the differences among cells and to explain their physiological behaviors at specific conditions.[18,19] Nevertheless, most commonly used cytomics approaches are still based on the static or destructive principle, yielding information at a single time point, or limited throughput, or a lack of precise extracellular environment manipulation. The cellular system in vivo (dynamic cytome, or also referred to as the cellome) is in a dynamic and complex environment, and the responses of cells to extracellular microenvironments (e.g., cell signaling) are also highly dynamic in time and space.[20,21] Therefore, in vitro reconstructing or simulating the physiological environment of the cell with spatial−temporal precision and probing single intracellular signaling dynamics with high throughput simultaneously may provide unprecedented insight into the underlying mechanisms of dynamic signaling networks.

An ideal platform for cellomics should show good capabilities in dimensions such as single-cell resolution, throughput, and dynamics (Figure 1a). Flow cytometry (Figure 1, parts a and b) is a powerful tool to achieve single-cell measurement with high throughput, but it cannot be used to probe time-dependent, transient cell responses to stimuli (without dynamics).[22] A multiwell microplate system (Figure 1, parts a and c) can observe cells over time with high throughput to obtain average dynamic information on large populations of cells, but lacks single-cell resolution. Optical microscopy (Figure 1, parts a and d) combined with the traditional perfusion strategy can be used to conveniently image the single-cell dynamics; however, it cannot quantify the fluorescence of thousands of cells at one moment under a fixed

Received: November 9, 2018
Accepted: December 17, 2018
Published: December 18, 2018

DOI: 10.1021/acs.analchem.8b05179
Anal. Chem. 2019, 91, 1619−1626

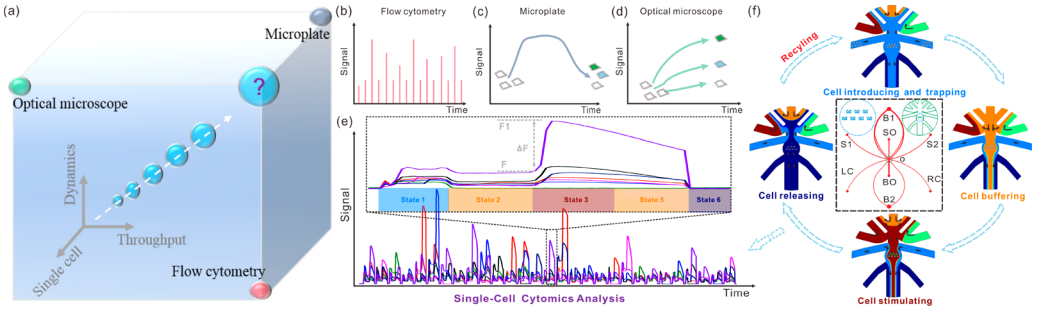

Figure 1. (a) Three-dimensional relation diagram of traditional methods for cell signaling analysis. (b–d) Typical signals obtained by flow cytometry, microplate, and optical microscope, respectively. (e) A typical trend of dynamic calcium signals of the Fluo-3/AM-loaded HeLa cells under ATP stimulation by dynamic microfluidic cytometry (DMC); enlarged graph of typical calcium signals, where F is the baseline signal, F1 is the maximum signal, and $\Delta F = F1 - F$. (f) The schematic diagram of DMC: cell introducing and trapping, cell buffering of obtaining signal baseline, accurately stimulating the cell with various chemical reagents, as well as real-time imaging and cell releasing.

field of view (limited throughput). These approaches have provided key insights into cellomics analysis at two aspects, but none of them can perform well at the third dimension simultaneously. Emerging microfluidics has been recognized as the next-generation instrumental platform and exhibits a strong ability for single-cell analysis, due to its features like smart individual cells handling with high throughput, precise fluid manipulation at high resolution, and miniaturized integration of different approaches.[23−39] Although it may add a new dimension to achieve cellomics based on microfluidic devices,[30,40−46] to obtain instantaneous dynamic information in a high-throughput manner for individual cells still remains a huge challenge.

In this paper, we report a novel microfluidic strategy and characterization protocol that is able to overcome the above-described challenges on time sensitivity, microenvironment control, throughput, and dynamic single-cell analysis by creatively applied cyclical cell trapping, stimulating, and releasing automatically, termed "dynamic microfluidic cytometry" (DMC) (Figure 1, parts e and f). By combining the advantages of flow cytometry, fluorescence microscopy, and microfluidics, the DMC could obtain high-throughput single-cell dynamics (single-cell cellomics) in an integrated platform.

EXPERIMENTAL SECTION

Chemicals and Reagents. Chemicals such as KCl, NaCl, HCl, $CaCl_2$, $MgCl_2$, NaOH, fluorescein, and D-glucose were purchased from Sinopharm Chemical Reagent (Shanghai, China). 4-(2-Hydroxyethyl)-1-piperazineethanesulfonic acid (HEPES), adenosine 5′-triphosphate disodium salt ($ATPNa_2$), histamine (HA), and acetylcholine chloride (ACH), penicillin, streptomycin, and dimethyl sulfoxide (DMSO) were purchased from Sigma-Aldrich (St. Louis, MO). Tyrode's solution (137 mmol L^{-1} NaCl, 5.4 mmol L^{-1} KCl, 1.3 mmol L^{-1} $CaCl_2$, 1.0 mmol L^{-1} $MgCl_2$, 10 mmol L^{-1} D-glucose, and 10 mmol L^{-1} HEPES) adjusted pH to 7.2 using NaOH was used for the buffer solution. Fluorescein was prepared in the buffer solution at a final concentration of 2×10^{-6} mol L^{-1}. $ATPNa_2$, HA, and ACH were dissolved in the buffer solution at a final concentration of 10−1000 μmol L^{-1} as the agonist, respectively. Fluo-3/AM (Biotium, Hayward, CA) stock solution in DMSO with a concentration of 2 mmol L^{-1} was diluted in buffer solutions at a final concentration of 10 μmol L^{-1}. All reagents were of analytical grade unless noted otherwise. All solutions were prepared with water purified by the Direct-Q system (Millipore, Bedford, MA) and filtered with 0.22 μm sterilized syringe filters prior to use.

Cell Culture and Preparation. HeLa and NIH-3T3 cells were obtained from the American Type Culture Collection (ATCC, Manassas, VA). Cells were cultured in 25 cm^2 tissue culture dishes 1−4 days prior to experiments with Dulbecco's modified Eagle's medium containing 10% (v/v) fetal bovine serum (Gibco), 100 μg mL^{-1} penicillin, and 100 μg mL^{-1} streptomycin, at 37 °C in a humidified atmosphere of 5% CO_2 in an incubator (Innova-Co 170; New Brunswick Scientific, Edison, NJ). The culture medium was changed at every 48 h. For subculture, cells were passaged at a ratio of 1:3 every 2 days to maintain cells in the exponential growth phase.

To measure Ca^{2+} concentration ($[Ca^{2+}]_i$), HeLa or NIH-3T3 cell suspensions were loaded with 10 μmol L^{-1} fluo-3/AM at 37 °C for 30 min. After dye loading, cells were centrifuged at 1000 rpm for 5 min in a 1.5 mL Eppendorf tube (Fisher Scientific, Hampton, NH, U.S.A.). After centrifugation, the supernatant was discarded and cells were then resuspended in Tyrode's solution at a specific concentration prior to use.

Chip Design, Fabrication, and Pretreatment. A poly(dimethylsiloxane) (PDMS)−glass hybrid microchip was designed and fabricated with a channel height of ≈30 μm, in which S1, S2, RC, LC, SO, BO, B1, and B2 corresponded to sample inlet 1, sample inlet 2, right cells inlet, left cells inlet, sample outlet, buffer outlet, buffer inlet 1, and buffer inlet 2, respectively (Figure S1a–c). The microfluidic chip was fabricated according to the rapid prototyping method. In brief, an SU-8 (GM1070, Gersteltec Sarl, Switzerland) mold was fabricated on a 3 in. silicon wafer substrate with standard soft-lithography technique. The PDMS layer, made from a mixture of base oligomers and curing agent in a mass ratio of 10:1, was fabricated by molding the SU-8 structure. After polymerization, the PDMS sheet was cut and peeled off from the mold. Access holes (2.0 mm in diameter) were punched at each end of the microchannel. The surface of the PDMS replica and a clean glass cover slide were treated with oxygen plasma treatment for 2 min (PDC-GC-M, Weike Spectrum, China) and immediately placed in physical contact with each other forming an irreversible seal. Quartz tubes (4 mm inner diameter and 12 mm height) were bonded upon the punched holes with AB glue as reservoirs to form the final device.

Before the experiment, the microchip was treated with oxygen plasma, added with 75% ethanol, and incubated in a clean bench at room temperature for 30 min. To reduce nonspecific adsorption during cell trapping, after the removal

DOI: 10.1021/acs.analchem.8b05179
Anal. Chem. 2019, 91, 1619−1626

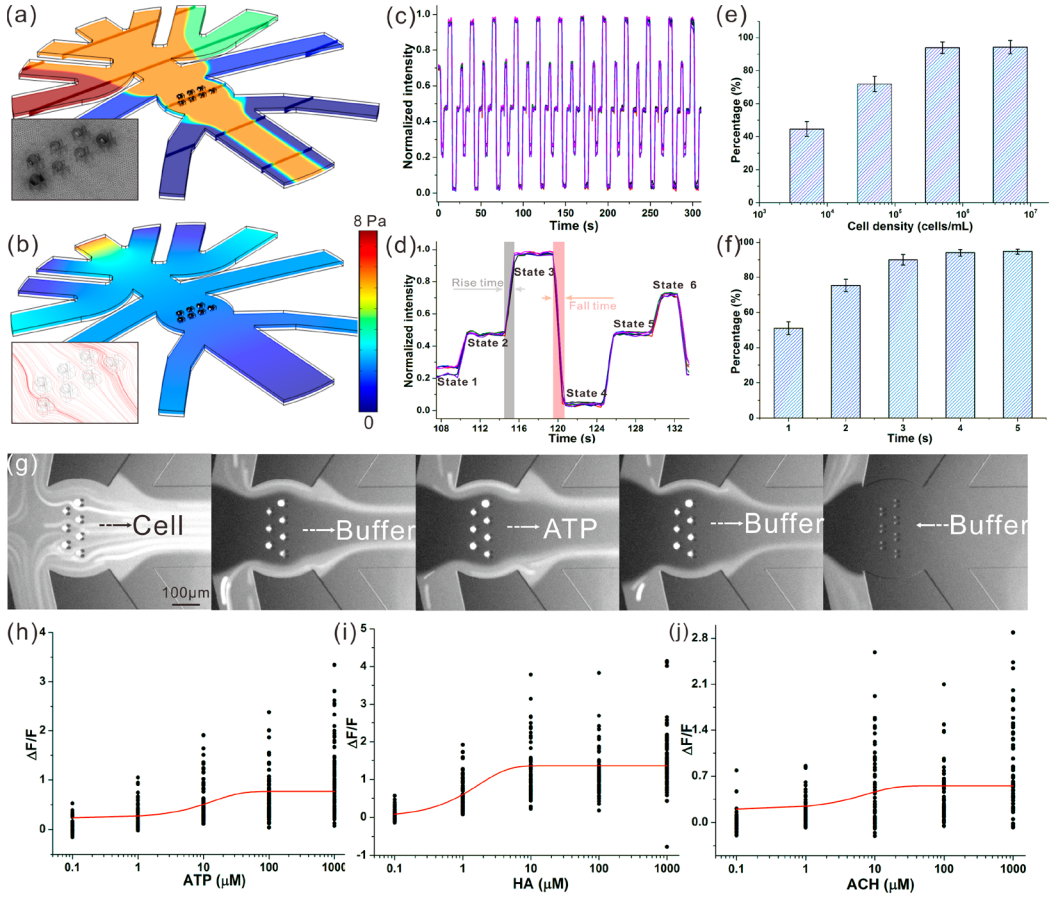

Figure 2. (a and b) Simulation results of the concentration (a) and shear stress distribution (b). The inset in panel a displays mesh grids for numerical simulation, and the inset in panel b shows the flow pattern field. (c and d) The repeatability of the proposed strategy. Repeated injections of fluorescein with times of each state of 3, 5, 5, 5, 5, and 2 s, respectively. The rise time and fall time are indicated as gray and red areas, respectively. (e and f) The trapping efficiency of cell density and cell introducing time. The standard error bars mean the variation of three individual experiments. (g) Visual representations for cell trapping, buffering, stimulating, and releasing in a typical cycle. (h–j) Dose–response curves to ATP stimulation (h), HA stimulation (i), and ACH stimulation (j), where the testing concentration range is 0.1–1000 μmol L^{-1} and each dot represents the response of a single cell.

of ethanol, the microchip was rinsed gently with buffer solution and 1 mg mL^{-1} bovine serum albumin (BSA) solution three times, sequentially.

Determination of the Single-Trapping Efficiency. Fluorescent polystyrene microbeads with diameters of 10 μm were purchased from the Research Institute of Chemical Engineering and Metallurgy (Beijing, China). Microbeads and undyed cells were loaded and introduced into microfluidic chips to test the single-trapping efficiency. Further, cell density and injection time were also optimized prior to real experiments. Image acquisition was begun upon beads/cells introduction and continued for the duration of the experiments.

Experimental Setup. All experiments were performed using an improved homemade pressure control system (Figure S1d), which included a microfluidic chip module, a pneumatic control module containing five independent electric/pneumatic (E/P) transducers (T-1001, Bellofram, U.S.A.), a LabView-based signal modulation module, and a microscopic imaging module. The pneumatic control module was utilized to precisely modify the pressures of the system, in which the E/P transducers could reduce an input pressure supplied by compressed nitrogen cylinder to a regulated output pressure directly proportional to a three-wire voltage input with 0.1% accuracy. All the operated E/P transducers were controlled by a PCI controller card (NI6703, National Instruments, Austin, TX) and a custom-designed LabView program. Experiments were carried out on an inverted fluorescence microscope (IX71, Olympus, Japan) with a CCD camera (Evolve 512, Photometrics, U.S.A.) for real-time image acquisition. The fluorescence signals were conducted with filter cubes of U-MWIB2 (460–490 nm band-pass filter, 505 nm dichroic mirror, 510 nm high-pass filter, Olympus, Japan) and finally monitored by a CCD camera. In addition, automated acquisition of bright-field and fluorescent cell imaging during the DMC, followed by off-line image processing and analysis using Image Pro Plus 6.0, Origin 7.5, Matlab, resulted in hundreds of dynamic single-cell responses.

Numerical Simulations. Numerical simulations were performed to examine the principle of DMC and to characterize the pressure distribution for the formation of DMC. Two-dimensional or three-dimensional numerical simulations were conducted using Comsol Multiphysics (COMSOL AB, Sweden) based on the finite element method. The flow patterns and the solution exchange of samples were characterized using the steady-state incompressible Navier–Stokes equation and the convective–diffusion equation. The corresponding equations were specified as follows:

DOI: 10.1021/acs.analchem.8b05179
Anal. Chem. 2019, 91, 1619–1626

$$\rho\frac{\partial u}{\partial t} + \partial u\cdot\nabla u = -\nabla p + \mu\nabla^2 u$$

$$\nabla u = 0$$

$$u\cdot\nabla c = d\nabla^2 c$$

where ρ, t, u, p, μ, d, and c are the density, time, velocity vector, pressure, dynamic viscosity, the diffusivity, and the concentration of the solution, respectively. The simulated fluid was Newtonian with ρ of 0.997×10^3 kg m^{-3} and μ of 0.895×10^{-3} Pa·s for pure water at 25 °C. The diffusivity of fluorescein solution of 500 μm^2 s^{-1} was used in our model. The boundary conditions for the fluid flow were set as follows: (i) no slip boundary conditions were applied on the walls; (ii) at each inlet, some other parameters, such as applied pressures and concentration of sample, were set according to the experimental data; (iii) pressure was set to zero at the outlet boundary.

RESULTS AND DISCUSSION

The typical trends of cell signaling over time of the Fluo-3/AM-loaded HeLa cells under ATP stimulation are shown in Figure 1e. The chip design and schematic of the system setup are shown in Figure S1. The proposed system setup contained a microfluidic chip, a custom-built multichannel pressure control module, and a LabView-based signal control module. The schematic representations shown in Figure 1f and Figure S1e demonstrate the proposed strategy. The evolution of DMC from a simple design into a highly integrated and complex system is shown in Figure S2. The DMC integrated the three typical steps in the loop on a microfluidic chip: (i) cell introducing and trapping, (ii) accurately stimulating the cell with various chemical reagents as well as real-time imaging, and (iii) cell releasing (Figure 1f). These three steps were divided into six states presented in Figure S1e: state 1 for cell introducing and trapping (in cyan), state 2 for cell buffering of obtaining signal baseline (in orange), state 3 for cell stimulating with one agonist (in red), state 4 for cell stimulating with another agonist (in green), state 5 for cell buffering again (in orange), and state 6 for cell releasing (in blue). A key experimental detail for fast releasing of cells was applying a transient high pressure in state 6, which is shown in the inset form of Figure S1e. The advantages of DMC were the provision of rich functionality by flexible combinations of different states, such as high-throughput of the same or different types of single-cell dynamics upon one agonist, and even sequential stimulation or simultaneous stimulation of different agonists.

To validate the feasibility of the proposed method, the flow profiles and mass transport in the device were characterized using both numerical simulations and flow visualization experiments. Two-dimensional (Figure 1f) and three-dimensional numerical simulations were conducted using Comsol Multiphysics (COMSOL AB, Sweden) based on the finite element method. The typical three-dimensional numerical simulation results of the concentration and shear stress distribution and flow patterns are shown in Figure 2, parts a and b. Under this pressure range, the maximum shear stress was calculated to be 2.1 Pa, which was harmless to HeLa and NIH-3T3 cells.[36,37] Meanwhile, the experimental results also indicated that the shear stress did not induce any significant changes in cell morphology and variations in intracellular Ca^{2+} concentration when the cell was stimulated with buffer solutions (state 2 in Figure 1d).

Flow visualization experiments were then carried out on an inverted fluorescence microscope to investigate the feasibility and repeatability of the proposed DMC. Fluorescein with four different concentrations was supplied to reservoirs S1, S2, B1, and B2, respectively, and another different concentration of fluorescein was supplied to reservoirs RC and LC. By changing the pressures on each port, repeated pulsing of fluorescein (time of each state was 3, 5, 5, 5, 5, and 2 s, respectively) was first carried out to study the repeatability of this strategy. A relative standard deviation (RSD) of 1.0% (n = 12) was observed for the peak height, indicating an outstanding repeatability (Figure 2, parts c and d, and Video S1). The rise time and fall times corresponding to 90% change in fluorescence intensity were 174.6 ± 0.5 and 194.5 ± 0.6 ms (n = 12), respectively (Figure 2d). In theory, the solution exchange time is related to the flow rate in the microchannel, and hence pressures on each entrance, which could be improved by flexible adjusting of the pressures. To further assess the flexibility of the developed strategy, microbeads and undyed cells were loaded into the device for investigations. As shown in Figure S3, parts a and b, a multibead−one-trap (because of the relatively small size of microbeads) or one-cell−one-trap trapping, stimulating, and releasing was successfully realized using the developed microfluidic system (Video S2). Critically, it also provided excellent control of the microenvironment around the cells by solution exchange without losing trapping except for cell releasing. In order to find an optimal trapping efficiency, cell introducing density and cell introducing time were also investigated. As shown in Figure 2, parts e and f, the optimal cell introducing density and time were 1×10^5 cells mL^{-1} and 3 s, respectively. In such conditions, cell trapping efficiency was nearly 100%.

To demonstrate the unique ability of the DMC to probe single-cell dynamics and dose−response curves in single-cell resolution with high throughput, we next applied the proposed DMC platform to quantify single-cell dynamics by introducing rapid, cyclical agonist exposures to HeLa cells. Calcium signaling of single cells was monitored in real time in response to three typical kinds of agonist: ATP, HA, ACH. Calcium signaling response to ATP, HA, and ACH was mediated by three different receptors: purinergic receptor (P2YRs), histamine receptors (H1Rs), and muscarinic acetylcholine receptors (mAChRs) endogenous expression in HeLa cells, respectively; all belong to the superfamily of G protein-coupled receptors (GPCRs).[47,48] Figure 1e presents a typical single-cell calcium signaling profile over time responding to an ATP solution of 10 μmol L^{-1}, in which heterogeneity in cellular responses upon stimulations was observed as expected. The time of each state was 3 s for trapping, 5 s for buffering, 5 s for stimulating, 5 s for buffering again, and 3 s for releasing, respectively. Figure 2g visually displays a typical trend of calcium signals in different times of the Fluo-3/AM-loaded HeLa cells under 10 μmol L^{-1} ATP stimulation. More importantly, the DMC facilitated rapid dose−response measurements in determining agonist efficacies and half-maximal effective concentration (EC50) values using serial dilutions of ATP, HA, and ACH in the concentration range of 10^{-1}−10^3 mol L^{-1} at single-cell resolution. The dose−response curves were successfully generated in Figure 2h−j, yielding EC50 values of 5.6 ± 0.2, 1.2 ± 0.05, and 5.3 ± 0.1 μmol L^{-1} for ATP, HA, and ACH, respectively, which was in accordance

DOI: 10.1021/acs.analchem.8b05179
Anal. Chem. 2019, 91, 1619−1626

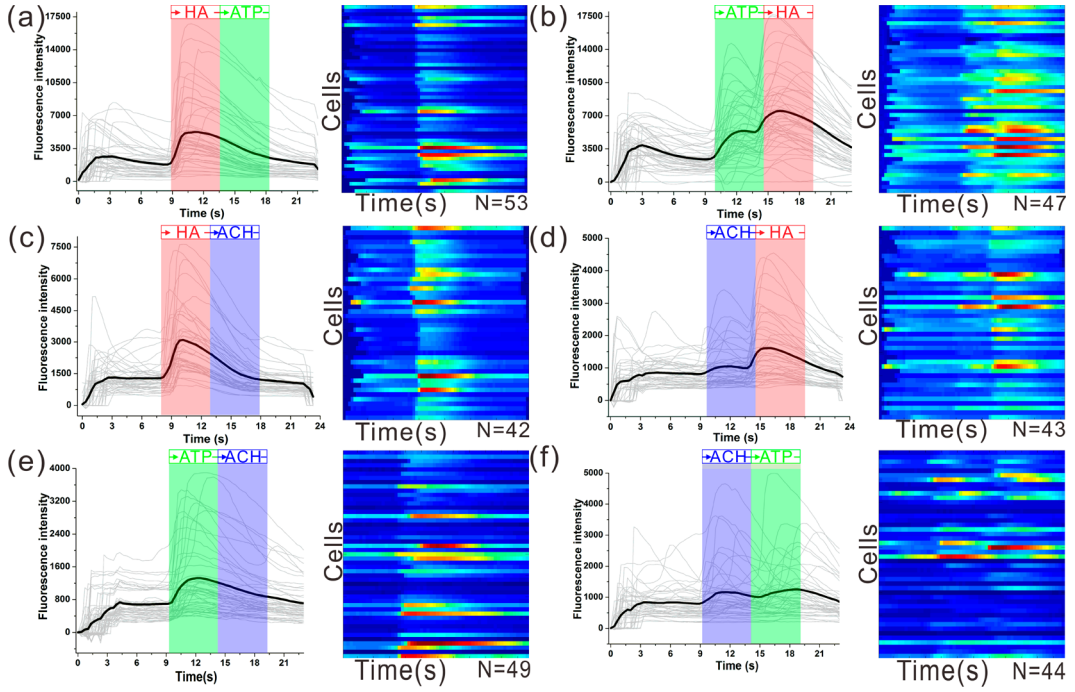

Figure 3. Tracking single-cell responses to sequential stimulation. (a–f) Time plots and heat maps showing the calcium signaling profiles of HeLa cells upon one agonist stimulation, followed by another agonist stimulation. The time courses of HA, ATP, and ACH stimulations are indicated as red, green, and blue areas, respectively. Each gray trace represents the response of a single cell, and black traces represent the average responses. Corresponding heat maps are shown to the right, each row corresponding to the calcium response of an individual cell, where blue indicates low calcium and red indicates high calcium. The ranges for the heat maps are the same as their corresponding time plots to the left. *N* represents the number of cells for which the responses are shown.

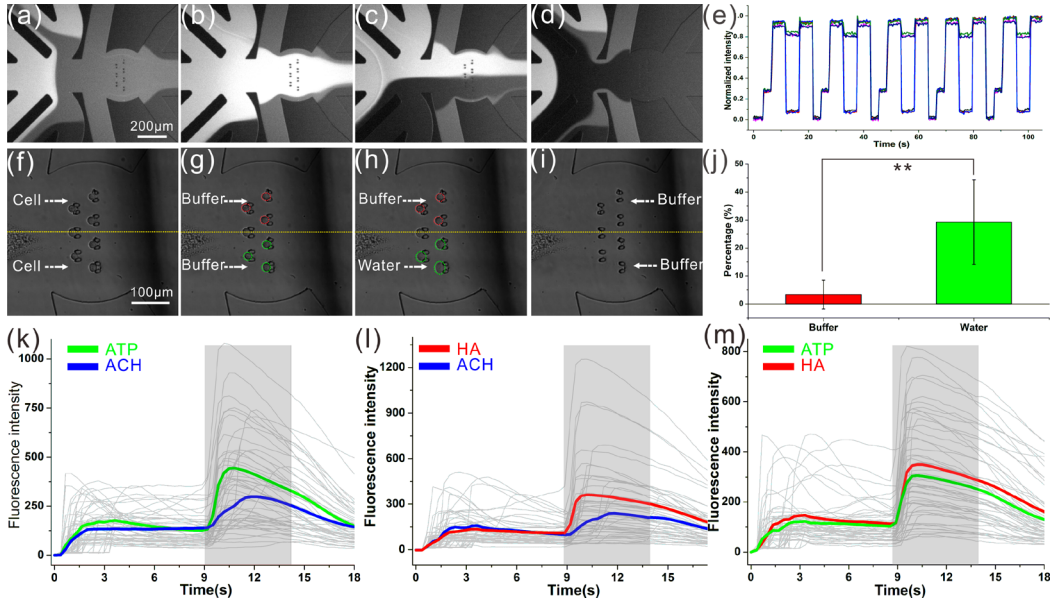

Figure 4. Tracking single-cell responses to simultaneous stimulation. (a–d) A typical flow pattern from a flow visualization experiment in different states in one cycle. Trapping different kinds of cells with 3 s (a), buffering with 5 s (b), simultaneous stimulating with 5 s (c), and releasing with 3 s (d). (e) Repeated injections of fluorescein with times of each state of 3, 5, 5, 5, and 3 s, respectively. (f–i) The typical morphological changes upon simultaneous water and buffer solution perfusion. (j) The statistical results of HeLa cells by two-way analysis of variance test (**$P < 0.01$). (k–m) The changes in fluorescence intensity of the cells over time to ATP and ACH (k), HA and ACH (l), and HA and ATP (m) stimulation. The gray shadings indicate the periods of stimulation. Each gray trace represents the response of a single cell, and color traces represent the average responses, where red, green, and blue lines denote the average responses to HA, ATP, and ACH, respectively.

with previous data of HeLa cells;[49−51] obviously, the data here provided more insights regarding the heterogeneity of single-cell dynamics. These results demonstrated the efficiency of our platform for monitoring single-cell dynamics and obtaining dose−response curves in a controlled manner at single-cell resolution.

Besides the single stimulation mentioned above, the ability of conveniently switching between different treatments enabled

DOI: 10.1021/acs.analchem.8b05179
Anal. Chem. 2019, 91, 1619−1626

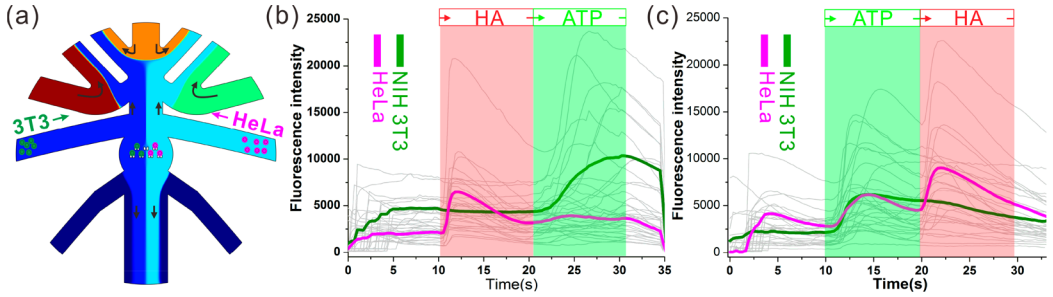

Figure 5. Single-cell dynamic signaling upon simultaneous stimulation to HeLa and NIH-3T3 cells. (a) The schematic diagram of simultaneous stimulation to HeLa (in pink) and NIH-3T3 cells (in olive) with the black arrows indicating the direction of the flow. (b and c) Time course of the fluorescence intensity upon simultaneous stimulation to HeLa and NIH-3T3 cells, where red and green areas indicate time courses of HA and ATP, respectively.

sequential stimulation or simultaneous stimulation, which allowed studies on different single-cell responses in dynamic environments. First, in order to characterize such different dynamics upon sequential stimulation, we cyclically trapped HeLa cells and perfused them with one agonist for 5 s, followed by another agonist for 5 s (detailed schematic shown in the principle for DMC), and monitored the $[Ca^{2+}]_i$ over time. As shown in Figure 3a, the perfusion of HA (10 μmol L^{-1}) to HeLa for 5 s caused a rapid rise in $[Ca^{2+}]_i$, and reached a maximum at a few seconds, but subsequent perfusion of ATP (10 μmol L^{-1}) could not induce another elevation in $[Ca^{2+}]_i$ (simplified representation: HA to ATP). Surprisingly, the responses of ATP to HA evoked different $[Ca^{2+}]_i$ changes from those evoked by HA to ATP. As shown, switching the order of such perfusion caused two remarkable responses in $[Ca^{2+}]_i$ during ATP to HA (Figure 3b). The similar results were obtained in other experiments presented in Figure 3c–f, where the cells were treated with sequential additions of HA to ACH and ACH to HA (Figure 3, parts c and d) or ATP to ACH and ATP to HA (Figure 3, parts e and f). Qualitative comparison of those responses revealed that different mechanisms were working in triggering intracellular calcium release. Depending on the class of the GPCRs involved, different downstream effectors would be activated in HeLa cells upon different agonist stimulation. A possible explanation was that the rank order of potencies of triggering calcium release from internal stores upon different agonists was HA > ATP > ACH.

On the basis of the unique ability of precise and dynamic control over a defined microenvironment around cells, we next applied this strategy to investigate the single dynamic signaling upon simultaneous stimulation. As shown in Figure 4a–d, by changing the pressures on each port, pulsing of fluorescein [time of each state was 3 s (trapping), 5 s (buffering), 5 s (simultaneous stimulating), 5 s (buffering), and 3 s (releasing), respectively] was successfully carried out, which indicated the feasibility of simultaneous stimulation of this strategy (Video S3). A relative standard deviation (RSD) of 1.1% (n = 5) was calculated for the peak height, demonstrating an outstanding repeatability (Figure 4e). In order to further characterize the superiority of the DMC to simultaneous dynamic change of extracellular environment, trapped HeLa Cells were simultaneously exposed to water and buffer solution and morphological changes were recorded to investigate cell responses to acute osmotic fluctuations. Figure 4f–i presents the typical morphological changes upon simultaneous water and buffer solution perfusion. As shown, only hypoosmotic shock generated by water could significantly induce a transient increase in cell body volume. Statistically, control cells introducing with buffer solution maintained constant cell shape volume (changed by an average of 3.3 + 5.1%), while hypoosmotic media (water) extended the diameter of cell body volume almost 10 times (changed by an average of 29.2 + 15.1%) when compared with the control group (Figure 4j). Two-way analysis of variance test indicated a significant effect of water treatment on cell body volume ($P < 0.01$) (Figure 4j). Subsequently, we attempted to use the DMC to monitor calcium signaling upon simultaneous stimulation to HeLa cells with different agonists. The results shown in Figure 4k–m summarize the changes in fluorescence intensity of the cells over time to 10 μmol L^{-1} ATP and 10 μmol L^{-1} ACH (Figure 4k), 10 μmol L^{-1} HA and 10 μmol L^{-1} ACH (Figure 4l), and 10 μmol L^{-1} HA and 10 μmol L^{-1} ATP (Figure 4m). Importantly, as shown in Figure 4k–m, the rank order of potencies of the maximum Ca^{2+} responses to agonists was also HA > ATP > ACH, which was consistent with the explanation shown in Figure 3. These results demonstrated the efficiency of our platform for monitoring single-cell dynamics upon sequential stimulation or simultaneous stimulation, which is potentially useful in online comparison of different agonists or drugs.

As mentioned above, simultaneous stimulation to two different cells was also theoretically possible by simultaneously introducing two kinds of cells in the state of cell introducing. The schematic representations shown in Figure 5a display such a proposed strategy, in which HeLa and NIH-3T3 cell suspensions were added to reservoirs RC and LC, respectively. After HeLa and NIH-3T3 cell introduction and successful trapping, we further attempted consecutive pulsing of HA and ATP solutions to trapping cells, and the time of each state was 3 s for trapping, 5 s for buffering, 10 s for stimulating with one agonist, 10 s for following by stimulating with another agonist, and 3 s for releasing, respectively. The intracellular calcium changes were monitored in real time, and the results are shown in Figure 5, parts b and c. Figure 5b shows the responses of HeLa and NIH-3T3 cells in the same condition. The application of 10 μmol L^{-1} ATP after the response to 10 μmol L^{-1} HA had no obvious effect on $[Ca^{2+}]_i$ level in HeLa cells, which is consistent with previous studies in Figure 3. NIH-3T3 cells displayed no response to HA (10 μmol L^{-1}) but very sensitive response to ATP (10 μmol L^{-1}). The underlying mechanism of such difference was that P2YRs endogenously expressed in NIH-3T3 cells but H1Rs did not. Further, switching the order of such perfusion induced predictable responses in $[Ca^{2+}]_i$ as shown in Figure 5c. We

DOI: 10.1021/acs.analchem.8b05179
Anal. Chem. 2019, 91, 1619–1626

believe that simultaneous quantification of dynamics to different kinds of cells using the DMC platform will play a critical role in furthering our understanding of single-cell dynamic signaling and offer insight into the efficacy of potential drug screening.

CONCLUSION

In summary, we have developed DMC for single-cell cellomics (cell signaling) analysis by creatively applied dynamic cell trapping and releasing automatically. Dose−response curves and EC50 values for HeLa cells treated with three different agonists were successfully obtained in single-cell resolution, which is also potentially suitable in other agonists or antagonists investigation. Single-cell dynamic signaling was further implemented by sequential stimulation or simultaneous stimulation. Simultaneous stimulation to two different cells has also proven to be attainable. These results revealed that the DMC provides a versatile means for probing single-cell signaling with high throughput, which is potentially useful in chemical biology, cell biology, and pharmacology research.

ASSOCIATED CONTENT

Supporting Information

The Supporting Information is available free of charge on the ACS Publications website at DOI: 10.1021/acs.analchem.8b05179.

Overall view of the microchannel with names for each entrance, the schematic representation of experimental setup, and the schematic diagram of DMC, evolution of DMC from a simple design into a highly integrated and complex system, and flow-visualized representations of beads and cells for trapping, buffering, stimulating, and releasing in a typical cycle (PDF)

Video of repeatability of the proposed strategy for cell trapping, buffering, stimulating, and releasing in a typical cycle (AVI)

Video of microbead or undyed cell trapping, stimulating, and releasing (AVI)

Video showing the single dynamic signaling upon simultaneous stimulation (AVI)

AUTHOR INFORMATION

Corresponding Author

*Phone: 86-27-8779-2203. E-mail: bfliu@mail.hust.edu.cn.

ORCID

Peng Chen: 0000-0002-2392-8106

Yiwei Li: 0000-0002-5203-0290

Bi-Feng Liu: 0000-0002-2135-0873

Author Contributions

†P.C. and S.Y. contributed equally to this work.

Notes

The authors declare no competing financial interest.

ACKNOWLEDGMENTS

We gratefully acknowledge the financial support from the National Natural Science Foundation of China (21775049, 31700746, 31870856, and 31870854), the National Key R&D Program of China (2017YFA0700403 and 2016YFF0100801), and the China Postdoctoral Science Foundation funded project (2018M630847 and 2018T110753).

REFERENCES

(1) Zahn, L. M. A. *Science* **2017**, *358*, 57−57.

(2) Pennisi, E. *Science* **2012**, *336*, 976−977.

(3) Han, X. P.; Wang, R. Y.; Zhou, Y. C.; Fei, L. J.; Sun, H. Y.; Lai, S. J.; Saadatpour, A.; Zhou, Z. M.; Chen, H. D.; Ye, F.; Huang, D. S.; Xu, Y.; Huang, W. T.; Jiang, M. M.; Jiang, X. Y.; Mao, J.; Chen, Y.; Lu, C. Y.; Xie, J.; Fang, Q.; et al. *Cell* **2018**, *172*, 1091−1107.

(4) Baslan, T.; Hicks, J. *Nat. Rev. Cancer* **2017**, *17*, 557−569.

(5) Macosko, E. Z.; Basu, A.; Satija, R.; Nemesh, J.; Shekhar, K.; Goldman, M.; Tirosh, I.; Bialas, A. R.; Kamitaki, N.; Martersteck, E. M.; Trombetta, J. J.; Weitz, D. A.; Sanes, J. R.; Shalek, A. K.; Regev, A.; McCarroll, S. A. *Cell* **2015**, *161*, 1202−1214.

(6) Zhang, K.; Gao, M.; Chong, Z. C.; Li, Y.; Han, X.; Chen, R.; Qin, L. D. *Lab Chip* **2016**, *16*, 4742−4748.

(7) Bendall, S. C.; Simonds, E. F.; Qiu, P.; Amir, E. A. D.; Krutzik, P. O.; Finck, R.; Bruggner, R. V.; Melamed, R.; Trejo, A.; Ornatsky, O. I.; Balderas, R. S.; Plevritis, S. K.; Sachs, K.; Pe'er, D.; Tanner, S. D.; Nolan, G. P. *Science* **2011**, *332*, 687−696.

(8) Li, Z. Y.; Huang, M.; Wang, X. K.; Zhu, Y.; Li, J. S.; Wong, C. C. L.; Fang, Q. *Anal. Chem.* **2018**, *90*, 5430−5438.

(9) Hughes, A. J.; Spelke, D. P.; Xu, Z. C.; Kang, C. C.; Schaffer, D. V.; Herr, A. E. *Nat. Methods* **2014**, *11*, 749−U794.

(10) Kang, C. C.; Yamauchi, K. A.; Vlassakis, J.; Sinkala, E.; Duncombe, T. A.; Herr, A. E. *Nat. Protoc.* **2016**, *11*, 1508−1530.

(11) Xu, F.; Zhao, H.; Feng, X. J.; Chen, L. H.; Chen, D. J.; Zhang, Y.; Nan, F. J.; Liu, J. F.; Liu, B. F. *Angew. Chem., Int. Ed.* **2014**, *53*, 6730−6733.

(12) Klein, A. M.; Mazutis, L.; Akartuna, I.; Tallapragada, N.; Veres, A.; Li, V.; Peshkin, L.; Weitz, D. A.; Kirschner, M. W. *Cell* **2015**, *161*, 1187−1201.

(13) Zhao, P.; Bhowmick, S.; Yu, J. C.; Wang, J. *Adv. Sci.* **2018**, *5*, 1800672.

(14) Pan, R. R.; Xu, M. C.; Burgess, J. D.; Jiang, D. C.; Chen, H. Y. *Proc. Natl. Acad. Sci. U. S. A.* **2018**, *115*, 4087−4092.

(15) Regev, A.; Teichmann, S. A.; Lander, E. S.; Amit, I.; Benoist, C.; Birney, E.; Bodenmiller, B.; Campbell, P.; Carninci, P.; Clatworthy, M.; Clevers, H.; Deplancke, B.; Dunham, I.; Eberwine, J.; Eils, R.; Enard, W.; Farmer, A.; Fugger, L.; Gottgens, B.; Hacohen, N.; et al. *eLife* **2017**, *6*, e27041.

(16) Chatterjee, M.; Acar, M. *Sci. Adv.* **2018**, *4*, e1701775.

(17) Mao, S. F.; Zhang, W. L.; Huang, Q. S.; Khan, M.; Li, H. F.; Uchiyama, K.; Lin, J. M. *Angew. Chem., Int. Ed.* **2018**, *57*, 236−240.

(18) Herrera, G.; Diaz, L.; Martinez-Romero, A.; Gomes, A.; Villamon, E.; Callaghan, R. C.; O'Connor, J. E. *Toxicol. In Vitro* **2007**, *21*, 176−182.

(19) Li, X. R.; Zhang, D. F.; Zhang, H. M.; Guan, Z. C.; Song, Y. L.; Liu, R. C.; Zhu, Z.; Yang, C. Y. *Anal. Chem.* **2018**, *90*, 2570−2577.

(20) O'Neill, P. R.; Giri, L.; Karunarathne, W. K. A.; Patel, A. K.; Venkatesh, K. V.; Gautam, N. *Wires Syst. Biol. Med.* **2014**, *6*, 115−123.

(21) Zhang, X. W.; Qiu, Q. F.; Jiang, H.; Zhang, F. L.; Liu, Y. L.; Amatore, C.; Huang, W. H. *Angew. Chem., Int. Ed.* **2017**, *56*, 12997−13000.

(22) Wu, H.; Wheeler, A.; Zare, R. N. *Proc. Natl. Acad. Sci. U. S. A.* **2004**, *101*, 12809−12813.

(23) El-Ali, J.; Sorger, P. K.; Jensen, K. F. *Nature* **2006**, *442*, 403−411.

(24) Wlodkowic, D.; Faley, S.; Zagnoni, M.; Wikswo, J. P.; Cooper, J. M. *Anal. Chem.* **2009**, *81*, 5517−5523.

(25) Dura, B.; Dougan, S. K.; Barisa, M.; Hoehl, M. M.; Lo, C. T.; Ploegh, H. L.; Voldman, J. *Nat. Commun.* **2015**, *6*, 5940.

(26) Di Carlo, D.; Wu, L. Y.; Lee, L. P. *Lab Chip* **2006**, *6*, 1445−1449.

(27) Zhang, K.; Chou, C. K.; Xia, X.; Hung, M. C.; Qin, L. *Proc. Natl. Acad. Sci. U. S. A.* **2014**, *111*, 2948−2953.

(28) Sumit, M.; Takayama, S.; Linderman, J. J. *Integr Biol-Uk* **2017**, *9*, 6−21.

(29) Wang, X.; Yi, L.; Roper, M. G. *Anal. Chem.* **2016**, *88*, 3369−3375.

DOI: 10.1021/acs.analchem.8b05179
Anal. Chem. 2019, 91, 1619−1626

(30) Chingozha, L.; Zhan, M.; Zhu, C.; Lu, H. A. *Anal. Chem.* **2014**, *86*, 10138−10147.
(31) Kaigala, G. V.; Lovchik, R. D.; Delamarche, E. *Angew. Chem., Int. Ed.* **2012**, *51*, 11224−11240.
(32) Ahmed, D.; Muddana, H. S.; Lu, M. Q.; French, J. B.; Ozcelik, A.; Fang, Y.; Butler, P. J.; Benkovic, S. J.; Manz, A.; Huang, T. J. *Anal. Chem.* **2014**, *86*, 11803−11810.
(33) Olofsson, J.; Bridle, H.; Sinclair, J.; Granfeldt, D.; Sahlin, E.; Orwar, O. *Proc. Natl. Acad. Sci. U. S. A.* **2005**, *102*, 8097−8102.
(34) Bennett, M. R.; Pang, W. L.; Ostroff, N. A.; Baumgartner, B. L.; Nayak, S.; Tsimring, L. S.; Hasty, J. *Nature* **2008**, *454*, 1119−1122.
(35) Dhumpa, R.; Truong, T. M.; Wang, X.; Roper, M. G. *Integrative biology: quantitative biosciences from nano to macro* **2015**, *7*, 1061−1067.
(36) Chen, P.; Guo, Y.; Feng, X.; Yan, S.; Wang, J.; Li, Y.; Du, W.; Liu, B. F. *Anal. Chem.* **2017**, *89*, 9209−9217.
(37) Chen, P.; Feng, X. J.; Chen, D. J.; Liu, C.; Du, W.; Liu, B. F. *Sens. Actuators, B* **2016**, *234*, 583−592.
(38) Kellogg, R. A.; Gomez-Sjoberg, R.; Leyrat, A. A.; Tay, S. *Nat. Protoc.* **2014**, *9*, 1713−1726.
(39) Li, Y.; Jang, J. H.; Wang, C.; He, B.; Zhang, K.; Zhang, P.; Vu, T.; Qin, L. *Adv. Biosys.* **2017**, *1*, 1700085.
(40) Bennett, M. R.; Hasty, J. *Nat. Rev. Genet.* **2009**, *10*, 628−638.
(41) Wang, Y.; Chen, Z. Z.; Li, Q. L. *Microchim. Acta* **2010**, *168*, 177−195.
(42) He, L.; Kniss, A.; San-Miguel, A.; Rouse, T.; Kemp, M. L.; Lu, H. *Lab Chip* **2015**, *15*, 1497−1507.
(43) Gonzalez-Suarez, A. M.; Pena-del Castillo, J. G.; Hernandez-Cruz, A.; Garcia-Cordero, J. L. *Anal. Chem.* **2018**, *90*, 8331−8336.
(44) Song, J.; Ryu, H.; Chung, M.; Kim, Y.; Blum, Y.; Lee, S. S.; Pertz, O.; Jeon, N. L. *Biosens. Bioelectron.* **2018**, *104*, 58−64.
(45) Chen, P.; Feng, X. J.; Yan, S. Q.; Guo, Y. R.; Wang, J.; Li, Y. W.; Chen, D. J.; Du, W.; Liu, B. F. *Sens. Actuators, B* **2018**, *263*, 281−288.
(46) Chen, P.; Guo, Y. R.; Wang, J.; Du, W.; Feng, X. J.; Liu, B. F. *Sens. Actuators, B* **2017**, *251*, 112−119.
(47) Haga, K.; Kruse, A. C.; Asada, H.; Yurugi-Kobayashi, T.; Shiroishi, M.; Zhang, C.; Weis, W. I.; Okada, T.; Kobilka, B. K.; Haga, T.; Kobayashi, T. *Nature* **2012**, *482*, 547−U147.
(48) De Backer, M. D.; Loonen, I.; Verhasselt, P.; Neefs, J. M.; Luyten, W. H. M. *Biochem. J.* **1998**, *335*, 663−670.
(49) Dolmetsch, R. E.; Lewis, R. S.; Goodnow, C. C.; Healy, J. I. *Nature* **1997**, *386*, 855−858.
(50) Sinclair, J.; Pihl, J.; Olofsson, J.; Karlsson, M.; Jardemark, K.; Chiu, D. T.; Orwar, O. *Anal. Chem.* **2002**, *74*, 6133−6138.
(51) Bootman, M. D.; Young, K. W.; Young, J. M.; Moreton, R. B.; Berridge, M. J. *Biochem. J.* **1996**, *314*, 347−354.

DOI: 10.1021/acs.analchem.8b05179
Anal. Chem. 2019, 91, 1619−1626